

Doppler imaging of stellar surface structure

XXIII. The ellipsoidal K giant binary ζ Andromedae^{*}

Zs. Kóvári¹, J. Bartus², K. G. Strassmeier^{2,**,***}, K. Oláh¹, M. Weber^{2,**,**}, J. B. Rice^{3,***}, and A. Washuettl^{2,**,**}

¹ Konkoly Observatory of the Hungarian Academy of Sciences, 1525 Budapest, Hungary
e-mail: [kovari;olah]@konkoly.hu

² Astrophysical Institute Potsdam (AIP), An der Sternwarte 16, 14482 Potsdam, Germany
e-mail: [jbartus;kstrassmeier;mweber;wasi]@aip.de

³ Department of Physics, Brandon University, Brandon, Manitoba R7A 6A9, Canada
e-mail: rice@BrandonU.ca

Received 5 July 2006 / Accepted 8 November 2006

ABSTRACT

Aims. We present the first Doppler images of the bright RS CVn-type binary ζ And. The star is a magnetically active K1 giant with its rotation synchronized to the 17.8-day orbital period. Our revised lithium abundance of $\log n = 1.2$ places ζ And in the vicinity of Li-rich RGB stars but it is nevertheless a Li-normal chromospherically active binary star. The star seems to undergo its first standard dredge-up dilution.

Methods. Four consecutive Doppler images were obtained from a continuous 67-night observing run at NSO-McMath in 1996/97. An additional single image was obtained from a continuous 19-night run at KPNO in 1997/98. These unique data allow to compute a small time series of the evolution of the star's surface structure. All line-profile inversions are done with a modified TempMap version that takes into account the non-spherical shape of the star. Representative test reconstructions are performed and demonstrate the code's reliability and robustness.

Results. High and low-latitude spot activity was recovered together with an asymmetric polar cap-like feature. The latter dominated the first half of the two-month time series in 1996/97. The second half showed mostly medium-to-high latitude activity and only a fainter polar spot. The coolest areas were restored with a temperature contrast of about 1000 ± 200 K. Some weaker features at equatorial latitudes were also recovered but these could be partially spurious and appear blurred due to imperfect phase coverage. We use our line profiles to reconstruct an average non-sphericity of $R_{\text{pole}}/R_{\text{point}} = 0.96$ which would, if not taken into account, mimic a temperature difference pole-to-equator of ≈ 220 K, especially at the phases of quadrature. Finally, we apply two different methods for restoring surface differential rotation and found a weak solar-type rotation law with a shear $\Delta\Omega \approx 0.95^\circ/\text{day}$ ($\alpha = \Delta\Omega/\Omega_{\text{eq}} = +0.049 \pm 0.003$), i.e. roughly a factor of four weaker at a rotation rate roughly 1.5 times faster than the Sun's.

Key words. stars: activity – stars: imaging – stars: individual: ζ Andromedae – stars: late-type – stars: starspots

1. Introduction

ζ And (HD 4502) is a long-period RS CVn-type single-lined spectroscopic binary with an orbital period of approximately 17.8 days. The binary nature was discovered by Campbell (1911) from variable radial-velocity measurements, which were completed by Cannon (1915) to give the first orbital solution. The spectral type has been classified as K1 III with a possible, but unseen, F companion on the basis of high-resolution optical spectra (Strassmeier et al. 1993, and references therein). The most recent orbital elements were computed by Fekel et al. (1999) based primarily on the data in the present paper.

* Figures A.1–A.3 and Table A.1 are only available in electronic form at <http://www.aanda.org>

** Visiting Astronomer, National Solar Observatory and Kitt Peak National Observatory, operated by the Association of Universities for Research in Astronomy, Inc. under contract with the National Science Foundation.

*** Based on observations obtained at the Canada-France-Hawaii Telescope (CFHT) which is operated by the National Research Council of Canada, the Institut National des Sciences de l'Univers of the Centre National de la Recherche Scientifique of France, and the University of Hawaii.

ζ And shows strong and variable Ca II H&K emission (Joy & Wilson 1949; Gratton 1950; Hendry 1980) that is interpreted to be due to chromospheric magnetic activity of the K giant. Ultraviolet spectra with IUE (Reimers 1980) and soft X-ray spectra obtained with *Einstein* (Schrijver et al. 1984) also suggested an overactive chromosphere and corona. ζ And was also detected in the ROSAT all-sky survey (Voges et al. 1999). However, strong H α absorption was reported by Fernández-Figueroa et al. (1994) and Eaton (1995). The star was listed among other radio sources in the survey of Drake (1989) and was also detected as a thermal infrared source by IRAS (Friedemann et al. 1996). The Li I-6708 line was detected by Randich et al. (1994) and a moderate logarithmic abundance of 0.9 derived (on the $\log n(\text{H}) = 12$ scale). The presence of lithium on the surfaces of giant stars provides constraints on its interior mixing processes along with its associated time scales and is therefore an important tracer of a star's evolutionary status.

Photometric light variations were first reported by Stebbins (1928). The amplitude of approximately 0.04 in *V* was interpreted to be due to an ellipticity effect of the giant component reaching between 80–100% of its Roche lobe (Hall 1990).

On the other hand, long-term changes of the light curve with a period similar to the orbital one suggested the existence of spot activity (Strassmeier et al. 1989, and references therein). This prompted us to monitor ζ And with high-resolution spectroscopy.

The main goal of this series of papers is to enrich the Doppler imagery of spotted stars of very different spectral types and of different evolutionary stages, which may allow us to find a relation between the spot distribution and a rotational or stellar-structure parameter. Moreover, detecting surface differential rotation or meridional flows from time-series Doppler images can give a direct quantitative input into the theory of stellar dynamos. In the earlier 22 papers we investigated altogether 23 stars, consisting 10 (effectively) single stars and 13 stars in close binaries, including 8 RS CVn systems. In our binary sample, ζ And is a unique system in the sense that this is the first system where strong ellipticity effect rules the photometric light curves. In Kóvári et al. (2005) a preliminary Doppler image of ζ And is presented from a subset of the data used in this paper, but with assuming spherical shape. However, because of the tidal distortion, a simple spherical model could obviously lead to an aliased surface temperature reconstruction and magnetic field strength as well (cf. Khalack 2005).

In this paper we present a new version of our Doppler-imaging code TEMP MAP that takes into account the distorted geometrical shape encountered for some ultra-rapidly rotating stars and evolved components in close binaries. We carry out numerical tests that allow an estimate of the expected impact of this effect (Sect. 3). In Sect. 5.1 we use the improved code to revise the Doppler image for 1997/98 and in Sect. 5.2 we present a new time-series of four Doppler maps covering 3.8 consecutive rotation periods of ζ And in 1996/97. A search for differential rotation using two different techniques as well as a search for meridional flows is presented in Sect. 6. Finally, Sect. 7 presents our conclusions.

2. Observations and numerical techniques

2.1. Optical spectroscopy at NSO, KPNO and CFHT

The bulk of the spectroscopic data, altogether 54 spectra covering 3.8 rotational periods, were collected at the National Solar Observatory (NSO) with the 1.5-m McMath-Pierce telescope during 67 consecutive nights between 3 November 1996 and 9 January 1997. We used the stellar spectrograph with the 800×800 TI-4 CCD camera at a dispersion of $0.10 \text{ \AA}/\text{pixel}$ and a resolving power of 42 000 as judged from the width of several Th-Ar comparison-lamp lines. The available spectral range of 6410–6460 \AA included the two primary mapping lines Fe I 6430 and Ca I 6439. An average exposure time of ≈ 90 s corresponds to a signal-to-noise (S/N) ratio of about 250:1 as measured in the continuum. Bias subtraction, flat-field division, wavelength calibration, and continuum rectification were performed on the raw spectra with the programs in IRAF (distributed by NOAO). Thorium-argon comparison spectra were obtained each night at intervals of one to two hours to ensure an accurate wavelength calibration.

A second set of data, altogether 14 spectra covering one single stellar rotation, was obtained at Kitt Peak National Observatory (KPNO) with the 0.9-m coudé feed telescope between 27 December 1997 and 15 January 1998. The TI-5 CCD detector was employed together with grating A, camera 5, the long collimator, and a $280\text{-}\mu\text{m}$ slit to give a resolving power of 38 000 at 6420 \AA . The wavelength range of these spectra

is 82 \AA and includes the mapping lines Fe I 6411 \AA , Fe I 6430 \AA and Ca I 6439 \AA . Exposure times were around 90 s. The average signal-to-noise ratio is $\approx 250:1$ in the continuum. Table A.1 in the appendix (available online) summarizes the mean HJDs and phases of all spectroscopic observations.

A single $R = 120\,000$ spectrum of the lithium 6708 \AA region was obtained with the $f/8$ *Gecko* spectrograph at the 3.6-m Canada-France-Hawaii Telescope (CFHT) on the night of 31 August 2004. In combination with the 4600×2048 $13.5 \mu\text{m}$ -pixel EEV1 CCD the spectrum covers a $100\text{-}\text{\AA}$ range centered at 6708 \AA and has a S/N of $\approx 300:1$ in the continuum.

2.2. Time-series photometry with APTs

Photometric data were collected with the T6 University of Vienna 0.75-m Automatic Photoelectric Telescope (APT) (Strassmeier et al. 1997) at Fairborn Observatory, Arizona between December 1996 and October 2002. The telescope was equipped with a blue-sensitive photomultiplier tube and Strömgren b and y filters and used HD 5516 as the primary comparison star (mean magnitudes of HD 5516 from SIMBAD are $V = 4^m.407$, $B - V = 0^m.943$, $U - B = 0^m.694$).

A total of 91 new by observations is presented. One observation consisted of three ten-second integrations on the variable, four integrations on the comparison star, two integrations on the check star, and two integrations on the sky. A $30''$ diaphragm was used. The standard error of a nightly mean from the overall seasonal mean was $0^m.003$ in b and y . For further details we refer to Strassmeier et al. (2000) and Granzer et al. (2001).

Additional BV photometry were used from Strassmeier et al. (1989) with an average standard deviation of ± 0.005 , and a single light curve (also in BV) from Zhang et al. (2000) with a probable error of ± 0.017 .

For phasing the data we go back to the orbital solution of Fekel et al. (1999) where T_0 is given as the time of maximum positive radial velocity. However, to fit the zero phase to the conjunction with the secondary in front we shifted T_0 by $0.25 \times P_{\text{orb}} = 4.442$ days and we used the following ephemeris to phase all of our data in this study (including spectroscopy):

$$\text{HJD} = 2\,449\,997.223 \pm 0.017 + 17.769426 \pm 0.000040 \times E. \quad (1)$$

2.3. Line-profile inversions with TEMP MAP

For the Doppler reconstruction in this paper we use the code TEMP MAP by Rice et al. (1989). The program performs a full LTE spectrum synthesis by solving the equation of transfer through a set of ATLAS-9 (Kurucz 1993) model atmospheres at all aspect angles and for a given set of chemical abundances. Simultaneous inversions of the spectral lines as well as of up to two photometric bandpasses are then carried out using a maximum-entropy regularization. Initially, we assumed solar abundances for all elements but converged on significantly subsolar abundances for both iron and calcium (-0.3 dex to -0.4 dex). To obtain a better fit for the main mapping line profiles, we altered the transition probabilities ($\log gf$'s) of some vanadium and titanium blends (see, e.g., Strassmeier et al. 1999 for a list of blends). A description of the TEMP MAP code and additional references regarding the inversion technique can be found in Rice et al. (1989), Piskunov & Rice (1993), Rice & Strassmeier (2000) and most recently in Rice (2002).

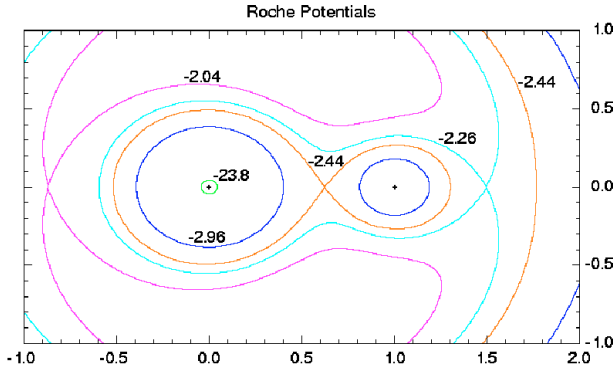


Fig. 1. Critical Roche equipotentials for the ζ And system. Shown are the stellar surfaces and the inner and outer critical equipotentials; L1 potential: -2.44 , L2 potential: -2.26 , surface potential of the primary: -2.96 , surface potential of the secondary in primary frame -23.8 . The K1III-primary component has a Roche lobe filling factor of 81%.

3. Towards Doppler imaging of an ellipsoidally distorted star

3.1. Initial guess of ζ And's non-sphericity

The ellipticity effect of ζ And has been studied by several authors fitting photometry with appropriate functions (e.g. $\sin \theta$, $\sin 2\theta$), summarized in Kaye et al. (1995). However, the star has also spots, possibly clustering around two preferred longitudes, as is observed on several other giants, e.g., on UZ Lib (Oláh et al. 2002a,b) or on IM Peg (Oláh et al. 2003). Therefore, a simple $\sin \theta$ or $\sin 2\theta$ fit to the light curve could not fully separate the ellipticity effect from effects of spots. To avoid this misinterpretation, we first predict the ellipsoidal light curve using the accurately determined stellar and orbital parameters in Sect. 4 and then iterate the true geometry within the line-profile inversion.

Figure 1 shows the location of the inner and outer critical equipotentials for the ζ And system as obtained with respect to the stellar surfaces. We used the program Nightfall as described by Wichmann (1998). Its light-curve prediction is shown in Fig. 2a along with our new y data and the V -band data from Strassmeier et al. (1989) and Zhang et al. (2000). The top curve is the expected ellipsoidal light curve. It shows a double-wave curve with unequal minima and with amplitudes smaller than quoted before by Kaye et al. (1995)¹. We obtained amplitudes for the stronger minimum of 0^m068 and 0^m062 in b and y , respectively and for the secondary minimum of 0^m056 and 0^m051 , again for b and y , respectively. Since the ellipsoidal curve was not fitted but predicted from the known stellar and orbital parameters, its uncertainty can only be estimated. The least known parameter is the inclination, which is determined from Doppler imaging as $65 \pm 5^\circ$ (cf. Fig. 5). For $i = 60^\circ$ the stronger minimum in y changes from 0^m062 to 0^m060 , and for $i = 68^\circ$ it changes to 0^m067 . (We note, that according to our new system geometry summarized in Table 2 at $i = 68^\circ$ a slight eclipse would appear). To sum up, we think that the uncertainty of the amplitudes of the ellipsoidal light curve are smaller than $\pm 0^m005$.

The expected Roche lobe filling factor for the primary component is of $\approx 81\%$. The secondary star is not seen in our spectra but is likely a late-G or early-K dwarf as deduced from the mass ratio and the mass function. We accept this, since the classification of the companion star (presumably F) in

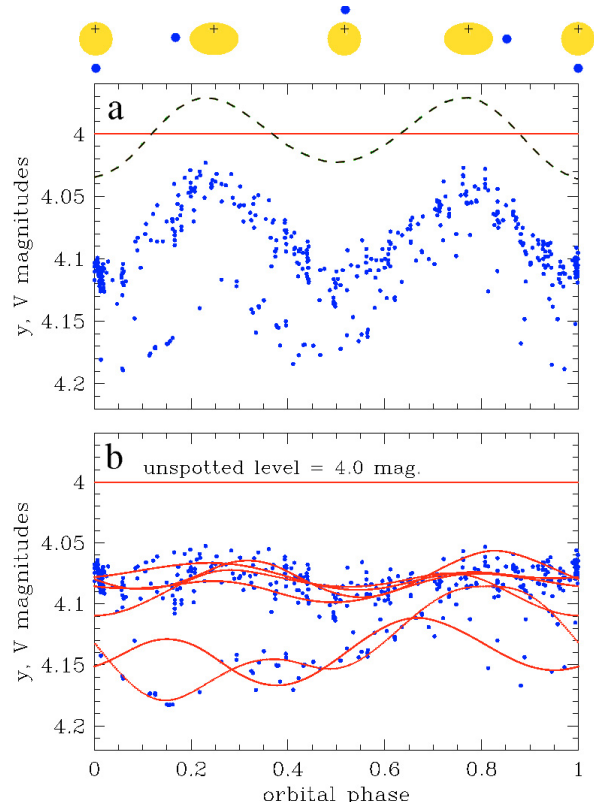


Fig. 2. a) V and y data of ζ And (points) and the calculated ellipsoidal light curve (dashed line) positioned at the unspotted light (full line). The graphics indicate the relative positions of the two stellar components. b) Same data but with the ellipticity effect removed. Note that the light minima still cluster around phases 0.00 and 0.50, the phases of conjunction. Also shown are the spot modelling fits for six different data segments. The upper four V light curves, taken from the literature, are observed in 1984 (a, b) and 1985 (Strassmeier et al. 1989) and in 1988 (Zhang et al. 2000), whereas the lower two curves are our new Strömgren y data from 1996/97. Note the vertical shift between the old and the new data, reflecting the long-term variability, a usual feature of active stars.

Strassmeier et al. (1993) was an initial guess based on visual inspection of the spectra.

3.2. Light curve spot modelling

Figure 2b shows the ellipticity-corrected magnitudes with numerous spot model fits from individual data sets. For the light curve correction we placed the expected ellipsoidal light curve at the supposed unspotted light level in such a way that its average value matches the unspotted level.

For modelling the data we used our code SPOTMODEL (Ribárik et al. 2003). The advantage of this program is that it treats two-color light curves simultaneously, and thereby fits the spot temperatures together with the spot position and size. The individual data sets and its fits are given in the online material in Fig. A.1. We allow for only two cool low-latitude spots with a fixed latitude of 25° (which is the center of the stellar disk at $i = 65^\circ$) and one at the pole which is adopted to account for the variable mean light level. The fits are very good (sum of squares of residuals range between 0.003 for the 1996 dataset to 0.011 for the 1985 dataset), which means that there is no major problem with the transformation between the Johnson and Strömgren systems. The spot coverage (in percent of the entire

¹ As mentioned in Fekel et al. (1999) the maximum spot amplitude of 0^m083 listed in Kaye et al. was a misprint.

Table 1. Spot modelling results.

Year	filter	spot temp. (K)	spot coverage (%)
1984a ^a	<i>B, V</i>	4247 ± 145	14.0
1984b ^a	<i>B, V</i>	4308 ± 82	16.1
1985 ^a	<i>B, V</i>	4438 ± 56	23.8
1988 ^b	<i>B, V</i>	3611 ± 104	6.2
1996 ^c	<i>b, y</i>	3480 ± 76	9.6
1997 ^c	<i>b, y</i>	3611 ± 198	10.8

^a Strassmeier et al. (1989); ^b Zhang et al. (2000); ^c present paper.

Table 2. System and stellar parameters for ζ And.

Parameter	Value
Classification	K1 III + K V
Period ^a , ($P_{\text{orb}} = P_{\text{rot}}$) [days]	17.769426 ± 0.000040
Eccentricity, e	0.0
Inclination, i [°]	65 ± 5
$v \sin i$ [km s ⁻¹]	41.4 ± 0.2
$a_1 \sin i^a$ [km]	6.14 10 ⁶
$a = a_1 + a_2$ [km]	3 10 ⁷ (2.7 R_*)
$f(m)^a$	0.0292
Mass ratio q (adopted) ^b	0.29
M_1 [M_\odot]	2.6 ± 0.4
M_2 [M_\odot] (adopted)	≈0.75
R_1 [R_\odot]	16.0 ± 0.2
Non-sphericity, ϵ (Eq. (2))	0.27 ± 0.04
$\log g$	2.8 ± 0.5
T_{eff} [K]	4600 ± 100
$(B - V)_{\text{Hipparcos}}$ [mag]	1.100 ± 0.004
$(V - I)_{\text{Hipparcos}}$ [mag]	1.06 ± 0.01
Distance _{Hipparcos} [pc]	55.6 ± 2.7
Microturbulence, ξ [km s ⁻¹]	1.0
Macroturbulence, $\zeta_{\text{R,T}}$ [km s ⁻¹]	2.0
[Fe/H]/[Fe/H] _⊙	-0.30 ± 0.05
[Ca/H]/[Ca/H] _⊙	-0.40 ± 0.05
$\log N(\text{Li})$ [H = 12]	1.24 ± 0.06

^a Fekel et al. (1999).

^b Stawikowski & Glebocki (1994).

hemisphere) and temperatures are given in Table 1. Due to the non-uniqueness of the solutions, we interpret them at least as evidence that the spot temperature varied between 3500–4400 K over the last two decades. Assuming no bright plages at all, in agreement with our Doppler imaging results, the spot coverage varied between 6–24% of the total stellar surface, being smaller with cooler spots and larger with less cool spots. On the Sun, larger spot coverage with lower contrast would indicate dissolving spots whereas smaller spot coverage and higher contrast would indicate newly emerged activity.

3.3. TEMP_{MAP}_ε: line-profile inversion with distorted geometry

We approximate the gravitationally distorted star with a rotational ellipsoid that is elongated towards the secondary star. We call this version furtherin TEMP_{MAP}_ε. This is a purely geometrical approach because it does not account for the effect of gravitational brightening of the poles or, equivalently, the darkening of the equatorial regions. E.g., the gravity ratio point-to-pole is 0.92 for 96% non-sphericity ($\epsilon = 0.27$ in Eq. (2)) and converts to an expected temperature gradient point-to-pole of ≈30 K from von Zeipel’s (1924) $T \propto g^{0.08}$ law. This is below the resolution capability of our data. Within reasonably small oblateness,

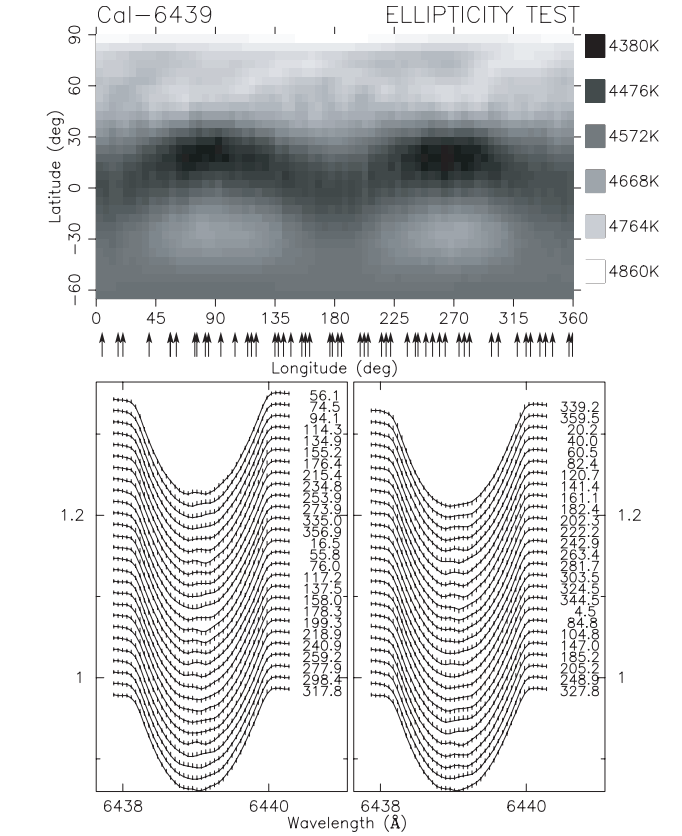


Fig. 3. The effect of neglecting the non-spherical shape of ζ And. *Top*: result from a spherical reconstruction of an artificial data set generated for an ellipsoidal star with a homogeneous surface temperature of $T_{\text{eff}} = 4600$ K and $\epsilon = 0.27$. All other parameters are as for ζ And in Table 2. The Doppler inversion transforms the phase-dependent geometry into hot and cool patches of $\Delta T \approx \pm 220$ K located preferentially at phase values of $\approx 90^\circ$ and $\approx 270^\circ$, i.e. the times of quadrature. *Bottom*: artificial spectra from the elliptical model (vertical dashes) with the corresponding phase values on the right and the fits (lines) from the inversion with a spherical model. Note that the profiles appear shifted vertically for better viewing.

we assume that gravity brightening per se can be neglected for our Doppler imagery.

Keeping the long radius of the star (the “point” radius) at unity, the short radius b is derived as

$$b = \sqrt{1 - \epsilon^2}, \quad (2)$$

where ϵ parameterizes the stellar distortion. Note that the radius for the poles is identical to the short radius b . This approximation is similar to Wood’s (1971) Roche approximation for light-curve modelling of detached and semidetached binaries. We emphasize that TEMP_{MAP}_ε is intended only for components in non-contact systems and/or for rotationally distorted stars but not for contact systems such as VW Cep or AE Phe (Hendry & Mochnecki 2000; Barnes et al. 2004).

3.4. Testing TEMP_{MAP}_ε

We first generate a series of synthetic spectra with the forward TEMP_{MAP}_ε version by assuming a homogeneous surface temperature of $T_{\text{eff}} = 4600$ K and $\epsilon = 0.27$. Then we reconstruct these data with the regular TEMP_{MAP} version employing an (inappropriate) spherical shape. The result is shown in Fig. 3. The spherical inversion perfectly fits the line-profile differences by

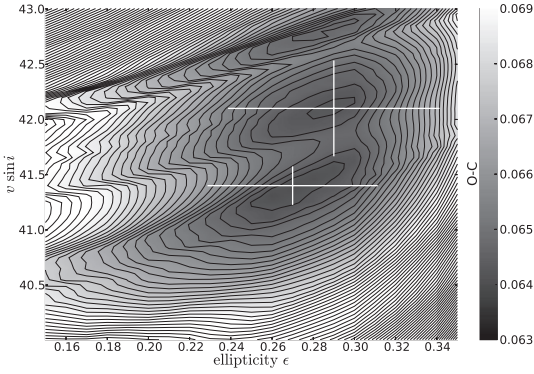


Fig. 4. Finding the optimal parameter combination for ellipticity (ϵ) and projected rotational velocity ($v \sin i$) from the Doppler-imaging procedure. Plotted are the χ^2 values over the $\epsilon - v \sin i$ cross-section of the parameter space using all the available NSO data. The main and the (slightly less significant) secondary minima marked with crosses correspond to the values of $\epsilon = 0.27 \pm 0.04$ with $v \sin i = 41.4 \pm 0.2 \text{ km s}^{-1}$ and $\epsilon = 0.28 \pm 0.05$ with $42.1 \pm 0.4 \text{ km s}^{-1}$, respectively.

creating cooler and hotter patches of up to $\Delta T \approx \pm 220 \text{ K}$ with respect to the effective temperature. Their location is preferably along the subobserver's latitude and at the visible rotational pole and piles up at the two phases of quadrature (the times of maximum projected stellar cross section). We conclude that neglecting the distortion can introduce an additional systematic error of up to several hundred degrees depending on the degree of distortion and on the inclination of the orbital plane with respect to the observer.

4. Fundamental stellar parameters for ζ And

4.1. The $\epsilon - i - v \sin i$ dependency

Through geometry, the distortion parameter ϵ is tightly connected to the projected rotational velocity $v \sin i$ and the inclination of the rotational axis i . For a star with $\epsilon > 0$ the quality of the line-profile fit with a spherical approximation would be phase dependent because, most easily imaginable for an edge-on orbit, the star would appear as a sphere during the times of conjunction and as a cigar during quadrature. Minimizing such a systematic effect in the residuals would result in the best value of the distortion. With this in mind, we scan through a meaningful part of the $v \sin i - \epsilon$ parameter plane obtained from many hundred inversions using the entire 1996/97 NSO data. Changing $v \sin i$ and ϵ , while all other parameters are held constant, yields the χ^2 map in Fig. 4. It indicates roughly a factor of two lower χ^2 than for inversions with $\epsilon = 0$, i.e., spherical approximation. The formal O–C minimum in Fig. 4 corresponds to $\epsilon = 0.27 \pm 0.04$ (polar radius of 0.96 if point radius is unity) and $v \sin i = 41.4 \pm 0.2 \text{ km s}^{-1}$. However, a second slightly less significant minimum is also apparent and corresponds to 0.28 ± 0.05 and $42.1 \pm 0.4 \text{ km s}^{-1}$, respectively. We note that the polar, point, and mean radii from the light-curve modelling in Sect. 3.1 are $15.93 R_{\odot}$, $17.22 R_{\odot}$ and $16.04 R_{\odot}$, respectively, and thus yield $\epsilon \approx 0.25 \pm_{0.04}^{0.07}$, in agreement with both minima from TEMPMAPE. For the future analysis we adopt the formally best value of $\epsilon = 0.27$.

The Doppler imaging procedure allows to determine some stellar parameters with better accuracy than with any other current method, such as i or $v \sin i$ (e.g. Unruh 1996; Weber & Strassmeier 1998). For example, varying the inclination of the stellar rotation axis while keeping the other parameters constant

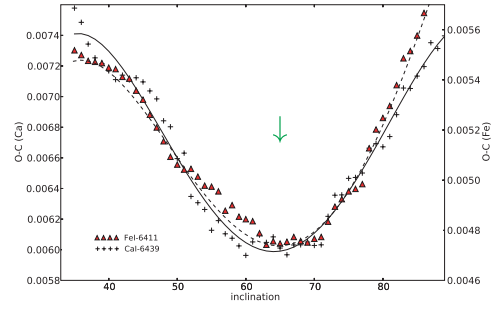


Fig. 5. Reconstructions of the surface temperature distribution for the 1997/98 data set with inclination angles of the stellar rotation axis between 35° and 90° . The vertical axis is reduced χ^2 as defined in Rice & Strassmeier (2000) for Ca (left) and Fe (right). Both lines suggest an inclination of $65 \pm 5^\circ$, just at the minimum of the two polynomial fits (solid line for Ca and dashed line for Fe).

yields the likely best estimate when the χ^2 of the line-profile fits reaches a minimum. The χ^2 distributions for the Ca I-6439 and Fe I-6411-lines are plotted in Fig. 5, where two respective minima are seen between 60° and 70° . Polynomial fits for both distributions yield 65° as the most likely inclination, in agreement with the upper limit of $\approx 71^\circ$ above which eclipses would occur (Stawikowski & Glebocki 1994). A lower limit of $i \approx 40^\circ$ is given from the constraint that the Roche lobe filling factor is < 1 (Hall 1990).

4.2. The unspotted magnitude

We adopted $V = 4^m 00$ as the unspotted light observed as maximum light in 2001. *Hipparcos*-Tycho lists $B - V = 1^m 100$, the same as observed in 1984–85 by Strassmeier et al (1989). Thus the unspotted B -magnitude is $B = 5.10$. However, our 1997/98 observations were made in Strömgren *by* and we must transform both the B magnitude of the comparison star and the unspotted B magnitude of ζ And to b . For this we used the method of Harmanec & Božić (2001) and derived a transformation formula especially for red stars with the author's original master table, and got $b = 4.679$ as unspotted light in Strömgren b . The error of the B -to- b transformation is expected to be less than $0^m 01$. Limb darkening coefficients were adopted from the tables of van Hamme (1993).

4.3. Mass, radius, luminosity

With the orbital elements $a_1 \sin i = 6.14 \times 10^6 \text{ km}$, $f(m) = 0.0292$ and $P_{\text{orb}} = 17.769426$ days from Fekel et al. (1999), together with the mass ratio of $q = 0.29$ and $M_1 = 2.7 M_{\odot}$ from Gratton (1950) and also adopted by Stawikowski & Glebocki (1994), and using $v \sin i = 41.4 \text{ km s}^{-1}$ from the present analysis, we obtain an independent guess for the inclination of $i = 64.6^\circ$, in very good agreement with the value of $i = 65^\circ$ found directly from Doppler Imaging (Fig. 5). The unprojected equatorial rotational velocity, and the fact that the rotational period appears synchronized to the orbital period, then suggests a likely radius of the primary of $R_1 = 16.0 \pm 0.2 R_{\odot}$.

With this radius and with $T_{\text{eff}} = 4600 \pm 100 \text{ K}$ from our photometry together with the *Hipparcos*-Tycho $B - V$ of $1^m 100$, we get $M_V = +0^m 14$ and $M_{\text{bol}} = -0^m 31$ by applying a bolometric correction of -0.45 from Bessell et al. (1998). The logarithmic luminosity of ζ And is then $\log L/L_{\odot} = 1.98 \pm 0.04$, based on an absolute bolometric magnitude of the Sun of $M_{\text{bol},\odot} = 4^m 74$ (Cox 2000). As a cross check, the apparent unspotted

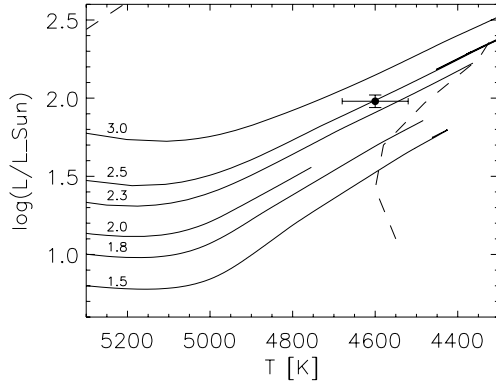


Fig. 6. The position of ζ And in the H-R diagram (dot) compared to evolutionary tracks from updated Kippenhahn tracks for $[\text{Fe}/\text{H}] = 0.0$. The bars emphasize the uncertainty and indicate a stellar mass of $2.5 \pm 0.4 M_{\odot}$. The dashed lines indicate the start of Li dilution (warmer line) while the cooler line indicates the deepest penetration of the convection zone (taken from Charbonnel & Balachandran 2000).

magnitude $V = 4^{\text{m}}00$ (Sect. 4.2) would require a distance of ζ And of 59.2 ± 3.7 pc in acceptable agreement with the *Hipparcos* value of 55.6 ± 2.7 pc if the radius is $16.0 R_{\odot}$.

Figure 6 shows ζ And in the H-R diagram with respect to the post-main-sequence evolutionary tracks from the Kippenhahn model (Kippenhahn et al. 1967). These models were updated with new physics in, e.g., Granzer et al. (2000) and were used by Holzwarth & Schüssler (2001). Shown are representative tracks for 1.5–3.0 solar masses and $[\text{Fe}/\text{H}] = 0.0$, i.e. solar abundances. ζ And’s position suggests a location on the red-giant branch (RGB) with a likely mass of $2.6 \pm 0.4 M_{\odot}$. The Schaller et al. (1992) tracks suggest $2.4 M_{\odot}$ while the Geneva-Toulouse tracks (Charbonnel & Balachandran 2000) suggest $2.7 M_{\odot}$, all with the same uncertainty of $\pm 0.4 M_{\odot}$. These masses are obtained from an interpolation between $[\text{Fe}/\text{H}] = 0.0$ and $[\text{Fe}/\text{H}] = -0.5$ tracks for a metallicity of -0.3 . All of above evolutionary codes include up-to-date input physics but no mixing other than convection, i.e. diffusion or rotational mixing. The warmer dashed line indicates the start of Li dilution and the cooler line indicates the deepest penetration of the convection zone (taken from Charbonnel & Balachandran 2000).

4.4. ζ And: a Li-rich RGB giant?

The CFHT high-resolution spectrum shown in Fig. 7 is used to obtain a revised Li abundance for ζ And. We first subtracted a shifted and rotationally broadened spectrum of the M-K standard star 16 Vir and then measured the residual equivalent width of 91 ± 3 mÅ. Its error is mostly set by the choice of the continuum and is an estimation from a number of trial continua. Note that the combined contribution of the many atomic and molecular blends within the full width of the Li line amounts to 40 mÅ. This equivalent width is obtained from two M-K standard stars of comparable spectral class and comes mostly from a Fe I + V I blend, as indicated in Fig. 7.

We assume that Li is purely ${}^7\text{Li}$. Then, the non-LTE curves of growth of Pavlenko & Magazzú (1996) for a 4600 K/ $\log g = 3.0$ model convert an equivalent width of 91 mÅ into a logarithmic Li abundance of 1.24 ± 0.06 (for LTE) and 1.58 ± 0.06 (for non-LTE), both on the $\log N(\text{H}) = 12.00$ scale. However, the non-LTE corrections interpolated from the results by Carlsson et al. (1994) were found to be so small (less than 0.03 dex) that we rather favor the LTE solution from Pavlenko & Magazzú (1996) and

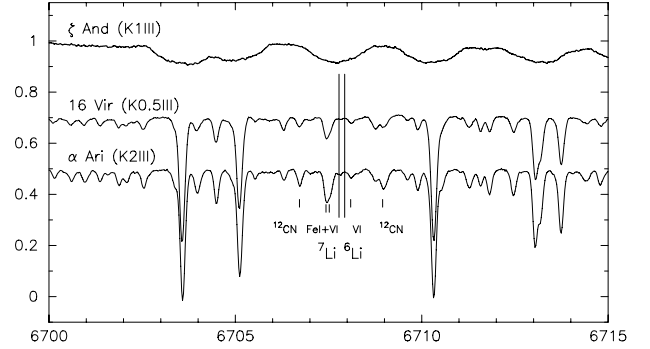


Fig. 7. Li I 6708 Å spectrum of ζ And (K1 III; top). Also shown are spectra of the M-K standards 16 Vir (K0.5 III; middle, shifted by -0.3) and α Ari (K2 III; bottom, shifted by -0.5). The equivalent width of the lithium line of ζ And minus 16 Vir is 91 ± 3 mÅ, corresponding to a logarithmic LTE abundance of 1.24.

neglect the non-LTE correction. In any case, our new abundance is significantly larger than the value of 0.9 given by Randich et al. (1994) based on an older equivalent width-temperature conversion with $T_{\text{eff}} = 4500$ K. Our new result places ζ And just in the vicinity of the group of abnormally Li-rich giants having $\log N(\text{Li}) > 1.4$ (cf. Charbonnel & Balachandran 2000) but is nevertheless a Li-normal chromospherically active binary that seems to undergo its first standard dredge-up dilution.

5. Doppler imaging of ζ And

5.1. A single Doppler image in 1997/98

The 14 spectra from the 1997/98 KPNO run span 19 consecutive nights, i.e. 1.07 stellar rotations, and allow the reconstruction of one Doppler image for each of the three main mapping lines. Adopting a distorted shape with $\epsilon = 0.27$ from Sect. 3.3, the restored 1997/98 maps and fits are shown in Fig. 8. The overall χ^2 as defined in Rice & Strassmeier (2000) is 0.0060, 0.0059, and 0.0047 for Ca I 6439 Å, Fe I 6430 Å, and Fe I 6411 Å, respectively, and is what we can expect from $S/N \approx 250:1$ spectra. No simultaneous photometry was available for this data set.

The three maps in Fig. 8 all show a cool polar cap-like spot together with numerous low-latitude spots. The polar spot and the coolest parts of other spotted regions have a temperature contrast of $\Delta T \approx 800$ – 1200 K with respect to the immaculate surface (4600 K). Despite that the Ca map shows similar features as the Fe maps, it appears generally cooler with a maximum contrast of more near ≈ 1200 K. This comes likely from the fact that the Ca I 6439 Å line has an intrinsically broader local line profile than the iron lines but is also very sensitive to temperature changes. Therefore, slightly wrong atomic and astrophysical parameters can have a more dramatic impact than for other lines with narrower profile. A number of weaker features is recovered as a band at lower latitudes. The detailed shape and location of these is likely spurious because they appear blurred due to the imperfect phase coverage. Their recovery must be judged unreliable.

The polar spot appears asymmetric with possibly two appendages. One smaller appendage at around $\ell \approx 30^\circ$ longitude and a broader one spanning ≈ 200 – 330° . The Fe-6411 line recovers the appendages with lesser contrast than the Ca line. Therefore, we use an average brightness map from the three lines to determine their contrast to be 750 ± 110 K. Similarly different contrasts from the Ca and Fe lines are noticeable at

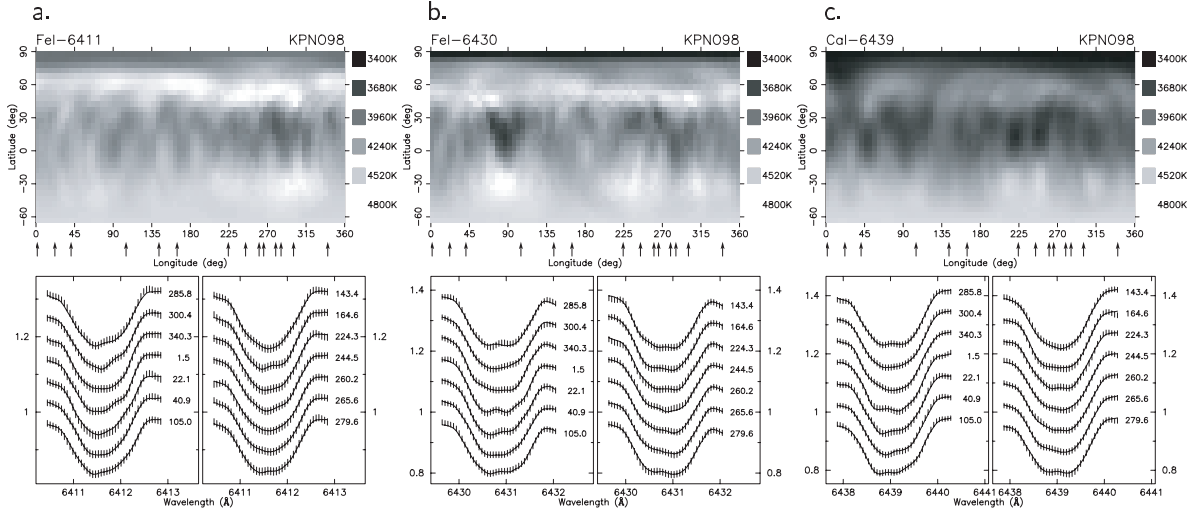


Fig. 8. Doppler images for one stellar rotation in December-January 1997/98 (KPNO data set). **a)** from FeI 6411 Å, **b)** from FeI 6430 Å and **c)** from CaI 6439 Å. The respective top panels show the temperature reconstructions. The arrows beneath the maps indicate the phase coverage while the lower panels show the line profiles and their fits. The profiles are numbered according to Eq. (1) in units of degrees from 0 to 360°. The vertical dashes are the observations with 1- σ error bars.

lower latitudes where two spotted regions at $\ell \approx 90^\circ$ (spot A) and $\ell \approx 270^\circ$ (spot B) appear in all three maps and dominate in the average brightness map. Their respective contrasts are 860 ± 220 K (spot A) and 1150 ± 110 K (spot B), on average. It seems plausible that these two spots are related to the position of the secondary star because $\ell = 90^\circ$ corresponds to a time of quadrature with the secondary receding, and $\ell = 270^\circ$ with the secondary approaching.

5.2. Time-series Doppler imaging in 1996/97

A total of 54 nightly NSO-McMath spectra from 67 consecutive nights, i.e. 3.77 stellar rotations, allowed the reconstruction of three independent maps plus a fourth one that has an overlap with the third map with its last three nights. The numbers of spectra per map is 14, 17, 15, and 11, respectively (see Table A.1 in the online appendix). Each map is made for the two main spectral lines Fe I 6430 Å and Ca I 6439 Å, the only ones available for this season due to the accidentally wrongly oriented CCD in the dewar. All stellar parameters were kept fixed for the line-profile inversions as for the KPNO data set and, again, a stellar distortion of $\epsilon = 0.27$ was adopted.

Figure 9a–d show the brightness average of the Fe I 6430 Å and Ca I 6439 Å reconstructions for the four data subsets. Individual maps are shown as part of the online material. The Ca-line’s fits overall χ^2 are 0.0097, 0.0139, 0.0137, and 0.0045 for maps #1–4, respectively, as compared to 0.0147, 0.0131, 0.0164, and 0.0079 for the respective Fe I 6430-Å fits. Simultaneous inversion of the photometry in two bandpasses is included in the overall χ^2 as prescribed by Rice & Strassmeier (2000).

As in 1997/98, the maps are dominated by an asymmetric polar cap-like spot with a temperature contrast of up to 1200 K. Its appendages appear to vary even from one rotation to the next. A monolithic appendage near $\ell \approx 160^\circ$ dominates in the first two rotations (Figs. 9a and b). By the third rotation the Ca line was reconstructed with mostly that particular appendage but decreased in contrast to $\Delta T \approx 1000$ K with the remaining parts of the cap at just ≈ 600 K. The Fe line, on the other hand, was reconstructed with a group of mid-latitude spots instead of the polar

appendage (a comparison of the individual maps is given in the appendix in Figs. A.2 and A.3). It appears that the entire polar feature became significantly weaker by the end of the time series and may even have vanished during the last of the four rotations (Fig. 9d). The individual Fe and Ca maps for rotation #4 remain inconclusive in this respect. While the Fe map still shows a polar feature with a just slightly reduced contrast of still 1000 K, the Ca lines were fit with only 600 K. We note that the *by* light curve during this time series shows subtle variations of its shape but in general remained dominated by its double-humped shape due to the ellipticity effect.

As in the KPNO data one year later, the NSO data also suggest low-to-mid latitude spots centered preferentially near the longitudes of quadrature. Numerous rather weak features with contrasts below ≈ 600 K appear as a low-latitude continuous band around the star. Note that such marginally constrained features usually are placed at or near the surface latitude that appears in the middle of the stellar disk, i.e. at $\approx 25^\circ$ in case of $i = 65^\circ$. This is part of the “dark side” of the minimum information principle applied in maximum-entropy line-profile inversions because it is the simplest solution. We caution the reader not to over-interpret these features despite their eye-catching appearance in Fig. 9.

6. Differential rotation and meridional flows

Differential rotation is one of the two key velocity patterns that drive the dynamo in stars with a convective envelope (the other is meridional circulation). Its full surface characterization including the sign is only possible once spatially resolved data like Doppler images are available. Although there is evidence for non-solar-like velocity patterns on very active giants, e.g. on σ Gem (Kóvári et al. 2001), UZ Lib (Oláh et al. 2002a) and HD31993 (Strassmeier et al. 2003), we presume a solar-type quadratic differential-rotation law of the form

$$\Omega(\theta) = \Omega_{\text{eq}} - \Delta\Omega \sin^2 \theta, \quad (3)$$

where θ is the stellar latitude, Ω_{eq} the equatorial angular velocity and $\Delta\Omega = \Omega_{\text{eq}} - \Omega_{\text{pole}}$. Other laws may be equally likely but could not be constrained with current data. In the following, we apply two different methods to recover Ω_{eq} and $\Delta\Omega$.

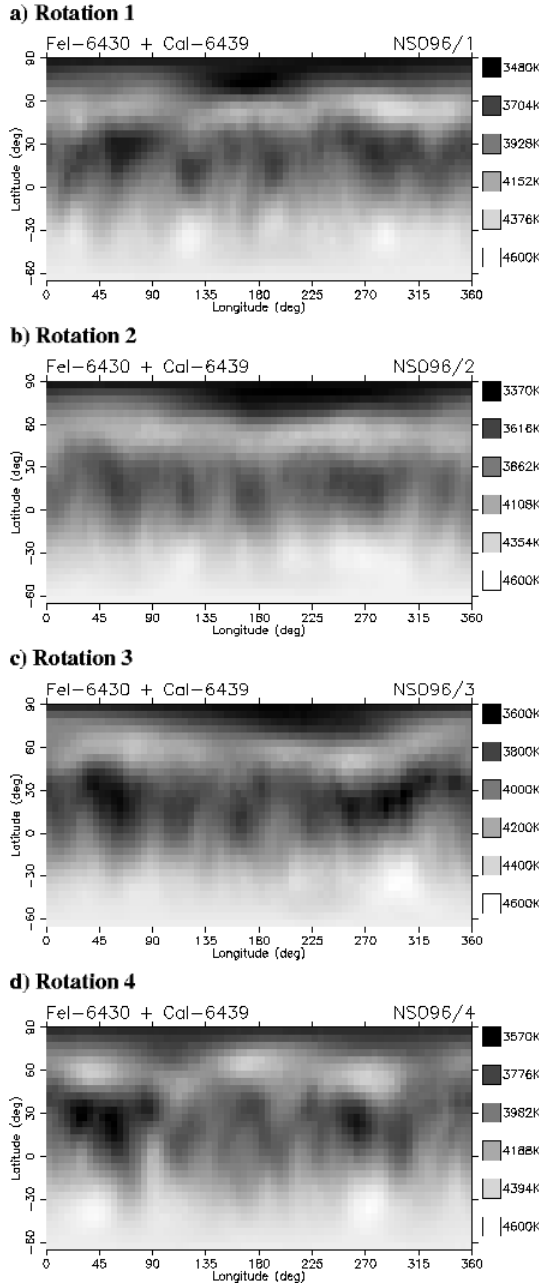


Fig. 9. Doppler images for four consecutive stellar rotations. The subsets **a)** NSO96/1, **b)** NSO96/2, **c)** NSO96/3 and **d)** NSO96/4 cover one stellar rotation each in November-January 1996/97. These temperature maps are obtained by brightness averaging the Fe I 6430 Å and Ca I 6439 Å images. Note that the image in **d)** has a 3-night overlap with the image in **c)** (phases 324.5°, 344.5°, and 4.5°). Strömgren *by* photometry was included in the line-profile inversion. Otherwise as in Fig. 8.

6.1. Sheared-image method

The sheared-image method includes above $\sin^2 \theta$ rotation pattern directly in the line-profile inversion code (see Barnes et al. 2005; Petit et al. 2002). Due to the already large number of free parameters in Doppler imaging, the image shear is introduced into TEMP MAP as a fixed parameter $\alpha = (\Omega_{\text{eq}} - \Omega_{\text{pole}})/\Omega_{\text{eq}}$ (Weber 2004). Computations are then done for a range of meaningful $\Omega_{\text{eq}} - \alpha$ pairs and the most likely value for α is again chosen on the basis of minimized χ^2 . This method also presumes a $\pm \sin^2 \theta$ law. The main advantage of the sheared-image method

is that only a single Doppler image is required to find α , while the cross-correlation method (Sect. 6.2) requires two consecutive images. The disadvantage is that it introduces yet another free parameter.

We apply the sheared-image method to the 14 spectra from the 1997/98 KPNO run that span a little over a stellar rotation. The method is thus well suited in this case because only a single Doppler image is available. The *S/N* ratio of this data set is also slightly better than for the NSO data set, which plays an important role due to the increased parameter space (Petit et al. 2004). TEMP MAP $_{\epsilon}$ with the sheared-image mode is applied separately to the Fe I 6411 Å, the Fe I 6430 Å, and the Ca I 6439 Å main mapping regions.

We first carry out a comparative test with the spherical and the non-spherical versions of TEMP MAP, both in sheared-image mode. The spherical version recovers the KPNO data set with an α of $+0.1^{+0.06}_{-0.03}$ and a rotation period of 18.02 ± 0.30 days. The minimum O–C was 0.0682 and 1- σ uncertainties would allow periods between 17.7 and 18.3 days and α between $+0.07$ and $+0.16$. The non-spherical version of TEMP MAP with its non-sphericity parameter ϵ set to zero (cf. Eq. (2)) recovers a perfectly identical χ^2 landscape, as it should, and verifies that no coding problem exists. Finally, we reconstruct the entire KPNO data set with $\epsilon = 0.27$ for periods between 17.2–18.3 days and α between -0.3 and $+0.3$. The resulting χ^2 landscape gives three local minima with periods of 17.42 ± 0.02 , 17.77 ± 0.02 , and 18.12 ± 0.04 days and α of $-0.1^{+0.05}_{-0.05}$, $-0.050^{+0.13}_{-0.03}$, and $+0.30^{+0.2}_{-0.15}$, respectively. The respective minimum O–C’s are 0.0632, 0.0641, and 0.066. Because only the 17.77-day period agrees with the orbital/rotational period of 17.769 days, we discharge the other two O–C minima. Still due to its large 1- σ width for α (-0.08 to $+0.08$), we must conclude that the sheared-image method does not yield a conclusive differential rotation determination from our data. We emphasize that this is not a failure of the method itself but due to its implicit character of the method on one hand and the non-sphericity of ζ And and the limited *S/N* of the KPNO data on the other hand.

6.2. Time-series cross-correlation method

The second method employs cross correlation of consecutive but contiguous maps from the time series in Sect. 5.2.

From the 54 NSO spectra, we formed 36 data subsets with 17 spectra in each. The first subset consists of the first 17 observations, the next subset is formed by omitting the first spectrum and adding the subsequent one to the end, etc., until the last 17 spectra are included. The result is a time series of altogether 36 Doppler-maps. In this way we reconstruct 36 maps independently for the 6430-Å iron line and for the 6439-Å calcium line and another 36 maps for the brightness averaged maps. We then consecutively cross correlate the independent maps, i.e. we compute a cross-correlation-function (ccf) map from image #1 and #17, then one from #2 and #18 and so forth until #19 and #36. This gives 19 ccf maps. Because the time baseline for these ccf maps varied between 18.09 and 20.46 days, we normalized the longitude shifts to the average time interval of 19.02 days, and then averaged the 19 ccf maps from both lines with equal weight. We then searched for a correlation peak in each longitude strip and fit a Gaussian to it (for a more detailed description of the procedure see, e.g., Paper V by Weber & Strassmeier 1998 and Paper XV by Kővári et al. 2001). The numerical correlation is done along longitude for all latitudes between -60° and $+85^\circ$ in bins of 5° . The longitudinal

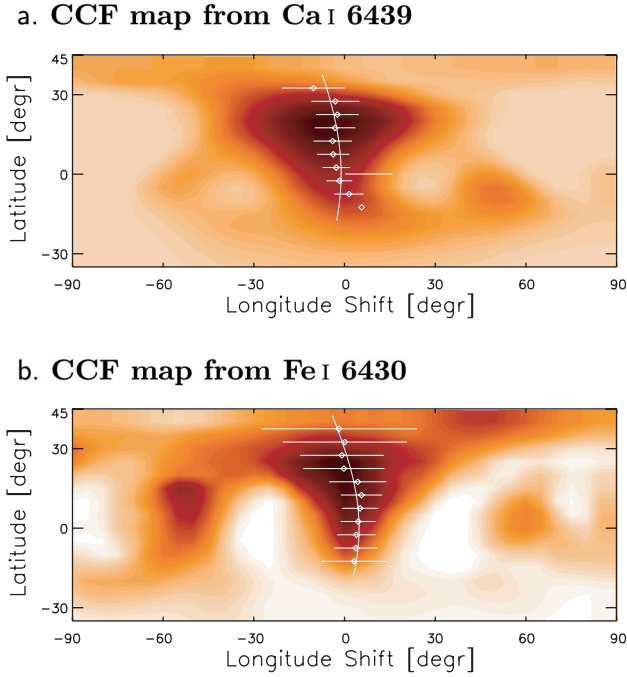


Fig. 10. Cross-correlation maps from the 1996/97 NSO time series. **a)** from the Ca-6439 maps, **b)** from the Fe-6430 maps. Black represents unity correlation, white no correlation. The dots with bars are the Gaussian-fitted correlation peaks per latitude bin and their root mean square. The full line is the best-fit solar-type differential rotation law and suggests a differential-rotation parameter $\alpha = \Delta\Omega/\Omega_{\text{eq}}$ of 0.046 from Ca and 0.053 from Fe.

distribution of the correlation is shown as subsequent latitude strips with grey scale in Fig. 10. For each strip the maximum correlation is represented by the Gaussian peaks (dots) and the corresponding FWHMs (bars). These bars are actually standard deviations from the 19 ccf maps and allow only an estimate of the true error. The Gaussian peaks were then fitted with the solar-type quadratic differential rotation law in Eq. (3). The two spectral lines yield

$$\text{for Ca : } \Omega(\theta) = 18.870 - 0.872 \sin^2 \theta \quad [^\circ/\text{day}], \quad (4)$$

and

$$\text{for Fe : } \Omega(\theta) = 19.183 - 1.019 \sin^2 \theta \quad [^\circ/\text{day}]. \quad (5)$$

Simple averaging yields a most likely differential rotation parameter $\alpha = \Delta\Omega/\Omega_{\text{eq}}$ of $+0.049 \pm 0.003$ (rms), which is one-quarter of the solar value of $+0.2$ at a rotation rate roughly 1.5 times higher than the Sun's. The shear $\Delta\Omega \approx 0.95^\circ/\text{day}$ (again the average from Eqs. (4) and (5)) is roughly a factor of two weaker than on the Sun. It translates into a lap time of ≈ 360 days, i.e. the time the equator needs to lap the pole by one full rotation.

6.3. Latitudinal cross-correlation

The cross-correlation method can also be applied to stellar latitude rather than longitude or phase as described in the previous paragraph. With such an analysis we hope to detect meridional velocity fields. Of course, only surface regions with spots would contribute to a cross-correlation signal. Therefore, what we aim to detect is simple latitudinal motion of spots that could be interpreted with a systematic meridional flow pattern.

As in Sect. 6.2, we cross correlate consecutive (contiguous) maps of the NSO time series. Altogether, 36 maps are used to

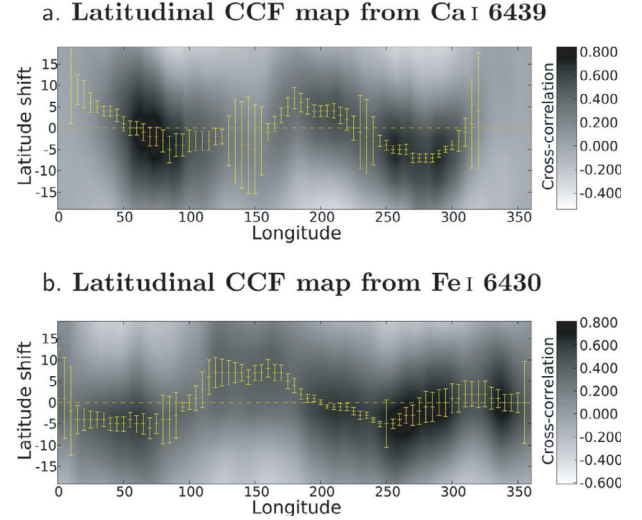


Fig. 11. Latitudinal cross-correlation maps from the 1996/97 NSO time series. **a)** from the Ca-6439 maps, **b)** from the Fe-6430 maps. Black represents unity correlation, white no correlation. The dots with bars are the Gaussian-fitted correlation peaks per longitude bin and their root mean square. Some common systematic changes appear in both panels, e.g. at longitudes of $\approx 70^\circ$ and between $250\text{--}300^\circ$, but are otherwise not entirely consistent and therefore likely spurious.

compute 19 latitudinal ccf maps; one from image #1 and #17, then one from #2 and #18 and so forth until the end of the time series. The numerical correlation was done along latitudes between 0° and 90° for all longitudes and is shown color/grey coded in Fig. 11. We then fit a 10th-order polynomial to the ccf function for each latitude strip and search for its maximum. The averaged maximum correlation per latitude bin is plotted as a dot in Fig. 11 while its standard deviation is represented as a bar calculated from the 19 ccf maps. It is a helpful measure but allows only an estimate of the true error. The latitudinal cross-correlation analysis was carried out for both the CaI-6439 and the FeI-6430 time series. Agreement between the two reconstructions exists in that the strongest correlations consistently appear at longitude $\approx 70^\circ$ and $\approx 250\text{--}300^\circ$ for a latitudinal equator-ward (negative) shift of $3\text{--}5^\circ$ during the time between the first and the last map (i.e. 19.02 days and therefore $\Delta\theta/\Delta t \approx 0.2^\circ/\text{day}$). However, the results are inconclusive in that the Fe reconstructions suggest a poleward flow pattern at $\approx 120\text{--}170^\circ$ while the Ca reconstructions suggest no or even equator-ward flow at these longitudes.

7. Summary and conclusions

Photometry and numerical line-profile simulations showed that ζ And's primary component is an ellipsoidal star with a pole to point radius ratio of 0.96. Taking this into account, our Doppler maps of ζ And revealed cool high-latitude and even polar spots with temperatures of about $800\text{--}1200$ K below the effective photospheric temperature. Evidence is presented that the polar spot faded by several hundred degrees within one to two stellar rotations during at least one occasion in 1996/97. It was again recovered with the previous contrast (1200 K) one year later from the KPNO data set. The low-latitude spots tended to group on the two hemispheres visible during quadrature, i.e. $\pm 90^\circ$ from the apsidal line following and preceding the location of the secondary star. This seemed to be the case for both observing seasons we had data for. At the same time the cool polar spot had

a large appendage near the phase of conjunction with the secondary behind in 1996/97, but less determinable in 1997/98. A comparable spot dependency on orbital location was seen on the active close binary σ^2 CrB (Strassmeier & Rice 2004). σ^2 CrB is a F9+G0 ZAMS binary. Cool spots appeared mainly at polar or high latitudes while a confined equatorial warm belt appeared on the trailing hemisphere of each of the two stars with respect to the orbital motion.

Application of two different techniques to determine the surface differential rotation law of ζ And gave consistent results but with inconclusively large error bars for the sheared-image method. Weber (2004) presented extensive numerical simulations with both methods and concluded that the sheared-image method generally gave more accurate reconstructions than the cross correlation technique. However, its success depends stronger on the S/N ratio of the data and its phase coverage than does the cross correlation method. Likely because of the additional complication due to the non-sphericity of ζ And the sheared-image method fails to reconstruct a unique differential rotation parameter from the single KPNO data set. The NSO time series has lower S/N and would be even more prone to ambiguities and we refrained from using it. However, the cross-correlation technique applied to the four consecutive stellar rotations covered by the NSO data set revealed a clear and unique differential-rotation signal. A fit with a solar-type quadratic law revealed a more rapidly rotating equator with a surface shear with respect to higher latitudes of four times lower than for the Sun and with a lap time of 360 days.

Rüdiger & Küker (2002) put forward gravity darkening as an explanation for the strong differential surface rotation of rapidly-rotating single active stars. Due to the rapid rotation a non-uniform heating from below is expected and would cause an equator-ward meridional flow, and thus an acceleration of the equatorial zones. In the case of a rapidly-rotating binary with a G or K-component like ζ And, stellar non-sphericity of several percent is sufficient to drive a much stronger meridional flow than on the Sun, that then would move large amounts of magnetic flux to preferred regions as observed. Whether the motion is clockwise or counterclockwise to the stellar rotation are currently open questions that we may solve by providing better observations of systems like ζ And or σ^2 CrB. Our current conclusion for ζ And is that there is evidence for both differential rotation and equator-ward meridional flows but also that these need independent verification to be conclusive.

Acknowledgements. We thank our referee for the useful comments which helped to improve the paper. Zs.K. is a grantee of the Bolyai János Scholarship of the Hungarian Academy of Sciences. Zs.K. and K.O. are grateful to the Hungarian Science Research Program (OTKA) for support under grants OTKA T-038013, T-043504 and T-048961. K.G.S. is very grateful to the Deutsche Forschungsgemeinschaft (DFG) for grant STR645 and to the Austrian Science Foundation (FWF) that made the original NSO observations in 1996/97 possible. This work was supported by the German-Hungarian S&T Bilateral Research Program 2002/2003. J.B.R. acknowledges support from the Natural Sciences and Engineering Research Council of Canada.

References

Barnes, J. R., Lister, T. A., Hilditch, R. W., & Collier Cameron, A. 2004, *MNRAS*, 348, 1321
 Barnes, J. R., Collier Cameron, A., Donati, J.-F., et al. 2005, *MNRAS*, 357, L1

Bessell, M. S., Castelli, F., & Plez, B. 1998, *A&A*, 333, 231
 Campbell, W. W. 1911, *Lick Obs. Bull.*, 6, No. 199, 140
 Cannon, J. B. 1915, *Publ. Dominion Obs. Ottawa*, II, No. 6, 141
 Carlsson, M., Rutten, R. J., Bruls, J., & Shchukina, N. G. 1994, *A&A*, 288, 860
 Charbonnel, C., & Balachandran, S. C. 2000, *A&A*, 359, 563
 Cox, A. N. ed. 2000, *Allen's Astrophysical Quantities* (New York: Springer)
 Drake, S. A., Simon, T., & Linsky, J. L. 1989, *ApJS*, 71, 905
 Eaton, J. A. 1995, *AJ*, 109, 1797
 ESA 1997, *The Hipparcos and Tycho catalog*, ESA SP-1200
 Fekel, F. C., Strassmeier, K. G., Weber, M., & Washuettl, A. 1999, *A&AS*, 137, 369
 Fernández-Figueroa, M. J., Montes, D., de Castro, E., & Cornide, M. 1994, *ApJS*, 90, 433
 Friedemann, C., Gürtler, J., & Löwe, M. 1996, *A&AS*, 117, 205
 Granzer, T., Schüssler, M., Caligari, P., & Strassmeier, K. G. 2000, *A&A*, 355, 1087
 Granzer, T., Reegen, P., & Strassmeier, K. G. 2001, *AN*, 322, 325
 Gratton, L. 1950, *ApJ*, 111, 31
 Hall, D. S. 1990, *AJ*, 100, 554
 Harmanec, P., & Bozic, H. 2001, *A&A*, 369, 1140
 Hendry, E. M. 1980, *PASP*, 92, 825
 Hendry, P. D., & Mochnacki, S. W. 2000, *ApJ*, 531, 467
 Holzwarth, V., & Schüssler, M. 2001, *A&A*, 377, 251
 Joy, A. H., & Wilson, R. E. 1949, *ApJ*, 109, 231
 Kaye, A. B., Hall, D. S., Henry, G. W., et al. 1995, *AJ*, 109, 2177
 Khalack, V. R. 2005, *A&A*, 429, 677
 Kippenhahn, R., Weigert, A., & Hofmeister, E. 1967, *Meth. Comp. Phys.*, 7, 129
 Kővári, Zs., Bartus, J., Strassmeier, K. G., et al. 2005, in *Cool Stars, Stellar Systems, and the Sun 13*, ESA-SP 560, 727
 Kővári, Zs., Strassmeier, K. G., Bartus, J., et al. 2001, *A&A*, 373, 199
 Kurucz, R. 1993, *ATLAS9 Stellar Atmosphere Programs and 2 km/s grid.*, CD-ROM No. 13 (Cambridge, Mass.)
 Oláh, K., Strassmeier, K. G., & Weber, M. 2002a, *A&A*, 389, 202
 Oláh, K., Strassmeier, K. G., & Granzer, T. 2002b, *AN*, 323, 453
 Pavlenko, Ya. V., & Magazzú, A. 1996, *A&A*, 311, 961
 Petit, P., Donati, J.-F., & Collier Cameron, A. 2004, *AN*, 325, 221
 Petit, P., Donati, J.-F., & Collier Cameron, A. 2002, *MNRAS*, 334, 374
 Piskunov, N. E., & Rice, J. B. 1993, *PASP*, 105, 1415
 Randich, S., Giampapa, M. S., & Pallavicini, R. 1994, *A&A*, 283, 893
 Reimers, D. 1980, in *2nd European IUE Conf.*, ESA SP-157, 77
 Ribárik, G., Oláh, K., & Strassmeier, K. G. 2003, *AN*, 324, 202
 Rice, J. B. 2002, *AN*, 323, 220
 Rice, J. B., & Strassmeier, K. G. 2000, *A&AS*, 147, 151
 Rice, J. B., Wehlau, W. H., & Khokhlova, V. L. 1989, *A&A*, 208, 179
 Rüdiger, G., & Küker, M. 2002, *A&A*, 385, 308
 Schaller, G., Schaerer, D., Meynet, G., & Maeder, A. 1992, *A&AS*, 96, 269
 Schrijver, C. J., Mewe, R., & Walter, F. M. 1984, *A&A*, 138, 258
 Stawikowski, A., & Glebocki, R. 1994, *Acta Astron.*, 44, 393
 Stebbins, J. 1928, *Publ. Washburn Obs.*, 15, 29
 Strassmeier, K. G., & Rice, J. B. 2004, *A&A*, 399, 315
 Strassmeier, K. G., Hall, D. S., Boyd, L. J., & Genet, R. 1989, *ApJS*, 69, 141
 Strassmeier, K. G., Hall, D. S., Fekel, F. C., & Scheck, M. 1993, *A&AS*, 100, 173
 Strassmeier, K. G., Boyd, L. J., Epan, D. H., & Granzer, T. 1997, *PASP*, 109, 697
 Strassmeier, K. G., Lupinek, S., Dempsey, R. C., & Rice, J. B. 1999, *A&A*, 347, 212
 Strassmeier, K. G., Granzer, T., Boyd, L. J., & Epan, D. H. 2000, *Proc. SPIE*, 4011, 157
 Strassmeier, K. G., Kratzwald, L., & Weber, M. 2003, *A&A*, 408, 1103
 Unruh, Y. C. 1996, in *Stellar Surface Structure*, ed. K. G. Strassmeier, & J. L. Linsky, *IAU Symp.*, 176, 35
 van Hamme, W. 1993, *AJ*, 106, 2096
 Voges, W., Aschenbach, B., Boller, T., et al. 1999, *A&A*, 349, 389
 von Zeipel, H. 1924, *MNRAS*, 84, 665
 Weber, M., & Strassmeier, K. G. 1998, *A&A*, 330, 1029
 Weber, M. 2004, Ph.D. dissertation, Universität Potsdam
 Wichmann, R. 1998, *Nightfall User Manual*, www.lsw.uni-heidelberg.de/rwichman/Nightfall.html
 Wood, D. B. 1971, *AJ*, 76, 701
 Zhang, Zh., Li, Yulan, Tan, Huisong, & Shan, Hongguang 2000, *IBVS*, 4935

Online Material

Table A.1. Mean HJDs, phases and image subdivisions of our spectra. Phases are from Eq. (1). NSO96 refers to the NSO McMath data from 1996/97 and the number 1–4 to the individual images. KPNO98 refers to the KPNO coude feed data from 1997/98.

HJD	phase	image
2450390.9194	0.1558	NSO96/1
2450391.8258	0.2068	NSO96/1
2450392.7942	0.2613	NSO96/1
2450393.7924	0.3175	NSO96/1
2450394.8117	0.3749	NSO96/1
2450395.8134	0.4312	NSO96/1
2450396.8579	0.4900	NSO96/1
2450398.7825	0.5983	NSO96/1
2450399.7410	0.6523	NSO96/1
2450400.6840	0.7053	NSO96/1
2450401.6709	0.7609	NSO96/1
2450404.6840	0.9304	NSO96/1
2450405.7678	0.9914	NSO96/1
2450406.7367	0.0460	NSO96/1
2450408.6766	0.1551	NSO96/2
2450409.6695	0.2110	NSO96/2
2450411.7056	0.3256	NSO96/2
2450412.7057	0.3819	NSO96/2
2450413.7173	0.4388	NSO96/2
2450414.7202	0.4952	NSO96/2
2450415.7555	0.5535	NSO96/2
2450416.7230	0.6079	NSO96/2
2450417.8130	0.6693	NSO96/2
2450418.7124	0.7199	NSO96/2
2450419.6352	0.7718	NSO96/2
2450420.6493	0.8289	NSO96/2
2450421.6085	0.8829	NSO96/2
2450422.6607	0.9421	NSO96/2
2450423.6663	0.9987	NSO96/2
2450424.6851	0.0560	NSO96/2
2450425.6626	0.1110	NSO96/2
2450426.6742	0.1680	NSO96/3
2450427.7568	0.2289	NSO96/3
2450429.6492	0.3354	NSO96/3
2450430.6693	0.3928	NSO96/3
2450431.6403	0.4474	NSO96/3
2450432.6946	0.5068	NSO96/3
2450433.6758	0.5620	NSO96/3
2450434.6589	0.6173	NSO96/3
2450435.6782	0.6747	NSO96/3
2450436.6931	0.7318	NSO96/3
2450437.5948	0.7825	NSO96/3
2450438.6706	0.8431	NSO96/3
2450439.7083	0.9015	NSO96/3, NSO96/4
2450440.6931	0.9569	NSO96/3, NSO96/4
2450441.6795	0.0124	NSO96/3, NSO96/4
2450445.6454	0.2356	NSO96/4
2450446.6315	0.2911	NSO96/4
2450447.6136	0.3464	NSO96/4
2450448.7135	0.4083	NSO96/4
2450450.5984	0.5143	NSO96/4
2450451.5888	0.5701	NSO96/4
2450453.7428	0.6913	NSO96/4
2450457.6412	0.9107	NSO96/4

Table A.1. continued.

HJD	phase	image
2450809.6889	0.7227	KPNO98
2450810.6465	0.7766	KPNO98
2450811.6758	0.8345	KPNO98
2450813.6427	0.9452	KPNO98
2450814.6903	0.2583	KPNO98
2450815.7055	0.0613	KPNO98
2450816.6361	0.1136	KPNO98
2450819.8002	0.2917	KPNO98
2450821.6960	0.3984	KPNO98
2450822.7408	0.4572	KPNO98
2450825.6868	0.6230	KPNO98
2450826.6835	0.6791	KPNO98
2450827.7257	0.7377	KPNO98
2450828.7232	0.7938	KPNO98

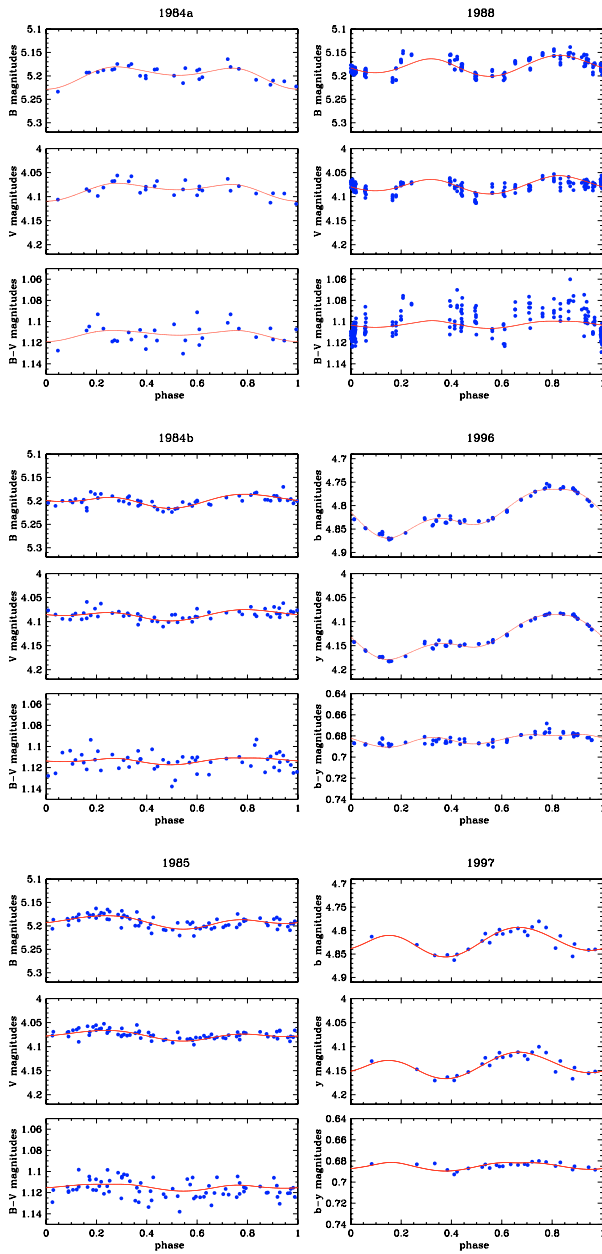


Fig. A.1. Fitted light and color curves of ζ And after removing the ellipsoidal variability. The upper border of the panels with V, y, B, b data represent the adopted unspotted light in these bandpasses.

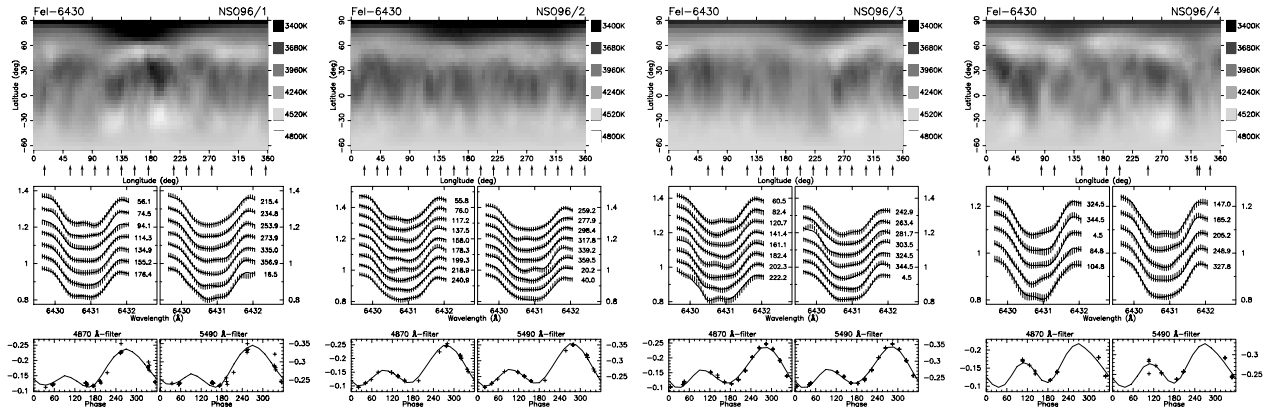


Fig. A.2. Fe I 6430 Å Doppler images for four consecutive stellar rotations (subsets NSO96/1, NSO96/2, NSO96/3 and NSO96/4) in November–January 1996/97.

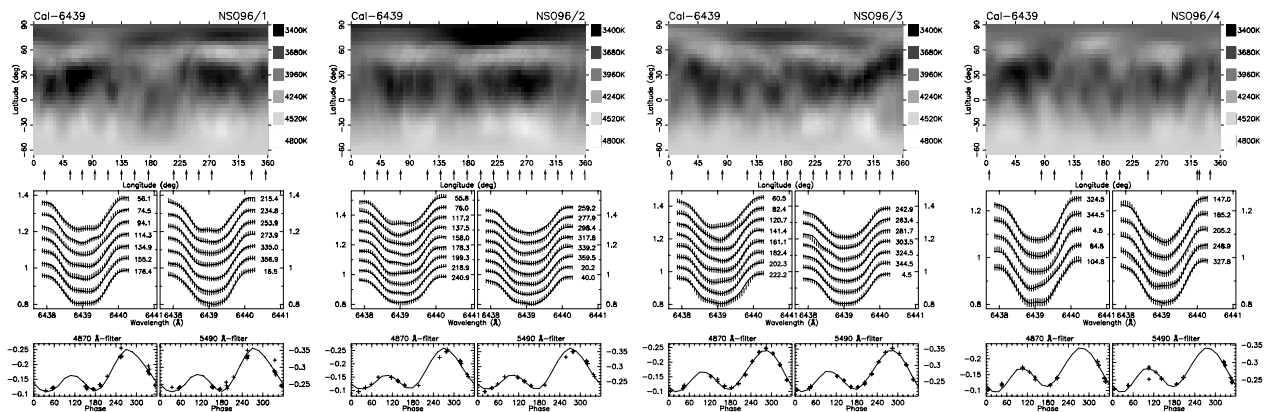


Fig. A.3. Ca I 6439 Å Doppler images for four consecutive stellar rotations (subsets NSO96/1, NSO96/2, NSO96/3 and NSO96/4) in November–January 1996/97.